Advances in Aircraft and Spacecraft Science, *Vol. 13, No. 1 (2026) 93-114*
https://doi.org/10.12989/aas.2026.13.1.093

Porosity induced variations in the mechanical response and stress evolution of Al-12Si/Al_2O_3 composite under thermo-mechanical loads

Billel Boukert[1a], Mohamed Khodjet Kesba*[1], A. Benkhedda[1b], E.A. Adda bedia[2]

[1]*Aeronautical Sciences Laboratory, Institute of Aeronautics and Space Studies, University of Blida 1, BP 270 Route de Soumaa, Blida 09000, Algeria*
[2]*Materials and Hydrology Laboratory, University of Sidi Bel Abbes, Algeria*

(Received June 17, 2025, Revised February 5, 2026, Accepted February 7, 2026)

Abstract. This study investigates the thermo-mechanical behavior of cracked and porous Al-12Si/Al_2O_3 metal-ceramic composites under varying thermal and mechanical conditions. A predicted model is developed to analyze stress distribution, Young's modulus, and Poisson's ratio while incorporating the effects of porosity and ceramic content. The results reveal that higher porosity weakens stress transfer and reduces stiffness, while increased ceramic content enhances rigidity but also intensifies stress localization. Young's modulus decreases significantly with temperature and porosity. Poisson's ratio decreases with rising temperature, confirming reduced lateral deformation resistance in more porous structures. The proposed model is validated against the Equivalent Constraint Model (ECM), showing strong agreement in stiffness degradation trends. This study extends previous research by integrating Knudsen's model into stress distribution analysis, providing a novel approach to quantify porosity effects in thermo-mechanical behavior. The findings contribute to optimizing metal-ceramic composites for high-temperature applications in aerospace and automotive industries, ensuring enhanced thermal and mechanical stability.

Keywords: meta/ceramic; porosity; stress distribution; thermal stress; young's modulus

1. Introduction

Metal matrix composites (MMCs) have gained significant attention in recent years due to their outstanding mechanical and thermal properties. The growing demand in the automotive and aerospace industries for lighter, stronger, and more thermally stable materials has motivated extensive research on MMCs to improve fuel efficiency, reduce emissions, and enhance performance [1]. Incorporating ceramic particles as reinforcements enhances the stiffness, hardness, and chemical stability of metallic matrices, combining the toughness of metals with the high strength of ceramics. Consequently, ceramic particle–reinforced metal matrix composites

*Corresponding author, Ph.D., E-mail: mkhojet@gmail.com
[a] Ph.D., E-mail: bilanosky@hotmail.fr
[b] Professor, E-mail: aaminabenkhedda@gmail.com
[c] Professor, E-mail: addabed@yahoo.com

http://www.techno-press.org/aas/5
ISSN: 2287-528X (Print), 2287-5271 (Online)

(CPMMCs) have become ideal materials for high-temperature components such as thermal barrier coatings, turbine blades, and piston rods [2].

In addition to conventional MMCs, interpenetrating metal–ceramic composites (IMCCs) have recently emerged as advanced materials offering superior thermo-mechanical properties. These composites are typically fabricated by infiltrating an open-porous ceramic preform with molten metal using processes such as pressure die casting, squeeze casting, or gas pressure infiltration, depending on the pore size and morphology of the ceramic network [2]. This infiltration-based approach provides improved load transfer and localized reinforcement without a significant density increase. Because of these advantages, metal–ceramic composites are increasingly used in high-temperature applications (450–500 °C), where understanding their thermal expansion and elastic behavior is crucial to ensure mechanical stability and control residual stresses [3], [4].

A number of studies have investigated the thermo-mechanical response of IMCCs. Schukraft et al. [2] demonstrated that an AlSi10Mg/ceramic foam composite with 74% open porosity exhibits nearly isotropic elastic behavior, with the elastic modulus decreasing from 110 GPa at room temperature to 80 GPa at 500 °C. Similarly, Sharma et al. [5] developed a 3D elastoplastic finite element model for Al/Al_2O_3 composites, accounting for residual stresses generated during sintering. Gudlur et al. [4] examined the influence of phase content, particle size, and porosity, confirming that smaller aluminum particles enhance density and stiffness while lowering the coefficient of thermal expansion (CTE). Wei et al. [6] further optimized the CTE of aluminum–ceramic composites using spark plasma sintering with ZrW_2O_8 phases, while Kursa et al. [7] proposed an optimization framework for designing Al_2O_3–Cu and Al_2O_3–NiAl composites balancing stiffness and thermal expansion.

Recent developments in modeling and manufacturing have expanded the understanding of microstructure–property relationships in these composites. Bhat et al. [8] used additive manufacturing to fabricate metal–ceramic composites with enhanced thermal stability, whereas Shekhawat et al. [9] reported that nano-sized ZrO_2 reinforcements in Al6061 composites significantly increase tensile strength and elastic modulus. Complementary research by Khodjet-Kesba et al. [10] analyzed the effect of nonlinear temperature and humidity gradients on cracked metal/ceramic sandwich plates, showing that environmental variations can strongly affect interlaminar stress and stiffness degradation. These studies collectively underline the importance of porosity, reinforcement ratio, and microstructural control in defining thermo-mechanical performance.

In parallel, probabilistic and micromechanical models have been developed to improve the predictive understanding of such materials. Maizia et al. [11] applied the Tsai–Wu failure criterion and Monte Carlo simulations to estimate failure probability in composite structures under hygro-thermo-mechanical loading. Kim et al. [12] proposed a micromechanical framework to analyze poroelastic behavior in decomposed composites, demonstrating how pore geometry influences stress concentration and strain energy density. Shi et al. [13] developed a mesomechanical model incorporating temperature-dependent softening and decomposition to predict stiffness degradation in FRP composites under combined thermal and mechanical loading.

Despite these advances, limited research has focused on the coupled influence of porosity and cracking on the thermo-mechanical response of metal–ceramic composites. Existing models often treat these effects separately, which limits their predictive accuracy in real materials where both defects coexist.

The present study addresses this gap by developing a predictive theoretical model for cracked and porous Al-12Si/Al_2O_3 composites under combined thermal and mechanical loading. The

model accounts for the interaction between porosity, damage density, and ceramic content to evaluate stress distribution, Young's modulus, and Poisson's ratio. Its predictions are validated against the Equivalent Constraint Model (ECM) [14], showing strong agreement in stiffness degradation trends. The results provide physical insight into the influence of porosity and ceramic fraction on stiffness loss and stress transfer, offering a framework for optimizing metal ceramic composites used in aerospace and automotive high-temperature environments.

2. Theoretical analysis

2.1 Stress functions for hybrid sandwich plate laminates

We investigate a laminated plate under uniaxial loading, assuming the presence of a transverse crack in the inner layer oriented along the x-axis. The laminated plate is characterized by the dimensions $2h_c$, representing the width of the inner ply; h_m, the width of the outer ply; and 2S, the spacing between adjacent cracks (refer to Fig. 1), in the formulas below, the inner layer is represented by the index "c" and the outer layer by "m".

For the sandwich plate, the overall equilibrium condition necessitates that

$$\sigma_x{}^{(m)} h_m + \sigma_x{}^{(c)} h_c = \sigma_x h, \tag{1}$$

Where h is the half thickness of the plate.

The stress functions $F^{(i)}(x,y)$ for each layer can be expressed as

$$F^{(i)}(x,y) = f^{(i)}(x).\, g^{(i)}(y)\,, \tag{2a}$$

$$g^{(m)}(y) = A^{(m)} \cdot (y-h)^2 + B^{(m)} \cdot (y-h) + C^{(m)}, \tag{2b}$$

$$g^{(c)}(y) = A^{(c)} \cdot y^c + B^{(c)} \cdot y + C^{(c)}\,, \tag{2c}$$

Where $A^{(i)}$, $B^{(i)}$, $C^{(i)}$ are functions to be determined and (i = m or c) denote the metal and ceramic layer,

From Eq. (2), the following equations are derived based on the stress expressions for each layer [15]

$$\sigma_x{}^{(i)} = \frac{\partial^2 F^{(i)}}{\partial y^2}\,, \tag{3a}$$

$$\sigma_y{}^{(i)} = \frac{\partial^2 F^{(i)}}{\partial x^2}, \tag{3b}$$

$$\tau_{xy}{}^{(i)} = -\frac{\partial^2 F^{(i)}}{\partial x \partial y}\,, \tag{3c}$$

In the absence of body forces, the stress expressions above inherently satisfy the equilibrium Eqs. [15]

$$\frac{\partial \sigma_x{}^{(i)}}{\partial x} + \frac{\partial \tau_{xy}{}^{(i)}}{\partial y} = 0\,, \tag{4a}$$

$$\frac{\partial \tau_{xy}{}^{(i)}}{\partial x} + \frac{\partial \sigma_y{}^{(i)}}{\partial y} = 0\,, \tag{4b}$$

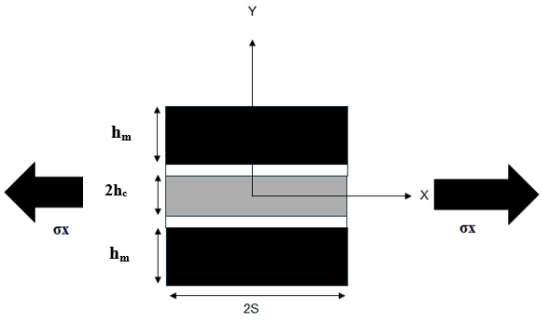

Figure 1. Composite sandwich plate laminate and geometric model

The conditions of traction continuity, boundary, and symmetry, as depicted in Fig. 1, necessitate that

$$\tau_{xy}{}^{(m)} = 0 \quad \text{at} \quad y = h, \tag{5a}$$

$$\sigma_y{}^{(m)} = 0 \quad \text{at} \quad y = h, \tag{5b}$$

$$\tau_{xy}{}^{(c)} = 0 \quad \text{at} \quad y = 0\,, \tag{5c}$$

$$\tau_{xy}{}^{(m)} = \tau_{xy}{}^{(c)} \quad \text{at} \quad y = h_c, \tag{5d}$$

$$\sigma_y{}^{(m)} = \sigma_y{}^{(c)} \quad \text{at} \quad y = h_c, \tag{5e}$$

$$u^{(m)} = u^{(c)} = 0 \quad \text{at} \quad x = 0, \tag{5f}$$

$$v^{(m)} = 0 \quad \text{at} \quad y = 0, \tag{5g}$$

$$\sigma_x{}^{(c)} = 0 \quad \text{at} \quad x = \pm S, \tag{5h}$$

$$\tau_{xy}{}^{(m)} = \tau_{xy}{}^{(c)} = 0 \quad \text{at} \quad x = 0, \pm S, \tag{5i}$$

By applying continuity conditions and substituting stress components, we derive Eqs. (6(a) and (b)), which describe stress variation across layers

$$A^{(m)} = 1, B^{(m)} = \ , C^{(m)} = 0\,, A^{(c)} = \ ?, B^{(c)} = 0, C^{(c)} = -h_c h\,, \tag{6a}$$

$$\left[f^{(m)}(x)\right]' = -\frac{h_c}{h1}\left[f^{(c)}(x)\right]', \left[f^{(m)}(x)\right]'' = -\frac{h_c}{h_m}\left[f^{(c)}(x)\right]'', \tag{6b}$$

When the self-equilibrium equation (Eq. (4)) is taken into account, (Eq. (6)) transforms into

$$f^{(m)}(x) = -\frac{h_c}{h_m} f^{(c)}(x) + \frac{h}{2h_c}\sigma_x\,, \tag{7}$$

From the above equations, one undetermined function can be obtained from the two stress functions.

$$f^{(c)}(x) = \phi(x), \tag{8}$$

The stress components for the metal layer are as follows

$$\sigma_x{}^{(m)} = 2\left[-\frac{h_c}{h_m}\phi(x) + \frac{h}{2h_m}\sigma_x\right], \tag{9a}$$

$$\sigma_y{}^{(m)} = (y-h)^2\left[-\frac{h_c}{h_m}\phi''(x)\right], \tag{9b}$$

$$\tau_{xy}{}^{(m)} = -2(y-h)\left[-\frac{h_c}{h_m}\phi'(x)\right], \tag{9c}$$

The stress components in the ceramic layer are as follows

$$\sigma_x{}^{(c)} = 2\phi(x), \tag{10a}$$

$$\sigma_y{}^{(c)} = (y^2 - hh_c)\phi''(x), \tag{10b}$$

$$\tau_{xy}{}^{(c)} = -2y\phi'(x), \tag{10c}$$

The strains in the inner and outer layers are derived from

$$\varepsilon_x{}^{(m)} = \frac{1}{E_x{}^{(m)}}\sigma_x{}^{(m)} - \frac{\upsilon_{xy}{}^{(m)}}{E_x{}^{(m)}}\sigma_y{}^{(m)} + \alpha_m\Delta T\,, \tag{11a}$$

$$\varepsilon_y{}^{(m)} = \frac{1}{E_y{}^{(m)}}\sigma_y{}^{(m)} - \frac{\upsilon_{xy}{}^{(m)}}{E_x{}^{(m)}}\sigma_x{}^{(m)}, \tag{11b}$$

$$\varepsilon_x{}^{(c)} = \frac{1}{E_x{}^{(c)}}\sigma_x{}^{(c)} - \frac{\upsilon_{xy}{}^{(c)}}{E_x{}^{(c)}}\sigma_y{}^{(c)} + \alpha_c\Delta T, \tag{11c}$$

$$\varepsilon_y{}^{(c)} = \frac{1}{E_y{}^{(c)}}\sigma_y{}^{(c)} - \frac{\upsilon_{xy}{}^{(c)}}{E_x{}^{(c)}}\sigma_x{}^{(c)}, \tag{11d}$$

By using the strain-displacement relationships in Eq. (11) and applying the displacement boundary conditions from Eqs. (5(f)) and (5(g)), the displacement fields are obtained as follows

$$u^{(m)} = \frac{2}{E_x{}^{(m)}}\left[-\frac{h_c}{h_m}\int\phi(x)\,dx + \frac{h}{2h_m}\sigma_x x\right] - \frac{\upsilon_{xy}{}^{(m)}}{E_x{}^{(m)}}\left[-\frac{h_c}{h_m}\int\phi''(x)\,dx\right](y-h)^2 + (\alpha_m\Delta T)x, \tag{12a}$$

$$v^{(m)} = -\frac{2\upsilon_{xy}{}^{(m)}}{E_x{}^{(m)}}\left[-\frac{h_c}{h_m}\phi(x) + \frac{h}{2h_m}\sigma_x\right]y + \frac{1}{E_y{}^{(m)}}\left[-\frac{h_c}{h_m}\phi''(x)\right]\frac{(y-h)^3}{3} + f(x), \tag{12b}$$

$$u^{(c)} = \left[\frac{2}{E_x^{(c)}}[\int\emptyset(x)dx] - \frac{\upsilon_{xy}^{(c)}}{E_x^{(c)}}\right][\int\emptyset''(x)dx](y-h_ch)^2 + (\propto_c\Delta T)x, \tag{12c}$$

$$v^{(c)} = -\frac{2\upsilon_{xy}{}^{(c)}}{E_x{}^{(c)}}\phi(x)\cdot y + \frac{1}{E_x{}^{(c)}}[\phi''(x)]\left(\frac{1}{3}y^3 - h_ch\cdot y\right), \tag{12d}$$

In Eq. (12(b)), $f(x)$ is a function which is determined by interface continuity conditions.

According to the model proposed by El Meiche et al. [16], we assume the existence of an inter-laminar isotropic resin layer with a thickness d, which separates the outer layer from the central layer. Poisson's ratio and transverse displacement effects are not considered; instead, the inter-laminar shear stress is calculated using the difference in average axial displacement [17]. The expressions for the average strains are derived from the angular deformation and displacement continuity between the two layers.

$$\overline{\varepsilon_y} = \frac{\partial \overline{v}}{\partial y} \approx \frac{v_m - v_c}{d} \,, \tag{13}$$

$$\overline{\upsilon_{xy}} = \frac{\overline{\partial u}}{\partial y} + \frac{\overline{\partial v}}{\partial x} \approx \frac{u_m - u_c}{d} + \frac{1}{2}\left(\frac{\partial v_m}{\partial x} + \frac{\partial v_c}{\partial x}\right), \tag{14}$$

Where u_m and v_m represent the displacements at the interface between the outer layer and the adhesive layer, and u_c and v_c denote the displacements at the interface between the central layer and the adhesive layer, d is the thickness of adhesive layer.

The inter-laminar stresses are determined using the linear stress–strain relationships

$$\sigma_y = E\,\frac{v_m - v_c}{d} \,, \tag{15}$$

$$\tau_{xy} = G\left[\frac{u_m - u_c}{d} + \frac{1}{2}\left(\frac{\partial v_m}{\partial x} + \frac{\partial v_c}{\partial x}\right)\right], \tag{16}$$

Where E and G represent the elastic moduli of the inter-laminar adhesive layer.

The function *f(x)* is determined by substituting Eqs. (12(b)) and (12(d)) into Eq. (15) with $y=h_c$. Subsequently, incorporating Eq. (12) and (16) yields

$$\tau_{xy} = G\left[\frac{u_m - u_c}{d} + \frac{\partial v_c}{\partial x} + \frac{d}{2E}\frac{\partial \sigma_y}{\partial x}\right] \,, \tag{17}$$

By substituting Eq. (12) and either (9(b)) or (10(b)) into Eq. (17) with $y=h_c$, we obtain

$$A\phi'''(x) + B\phi'(x) + C\int \phi(x)\,dx = Dx \,, \tag{18}$$

Where

$$A = G\left(\frac{\frac{1}{3}h_c^3 - hh_c^2}{E_y^{(c)}} + \frac{1}{2}\frac{d\left(h_c^2 - hh_c\right)}{E}\right) \,, \tag{19}$$

$$B = G\left(\frac{\frac{v_{xy}^{(c)}\left(h_c^2 - hh_c\right)}{E_x^{(c)}} + \frac{v_{xy}^{(1)} h_c (h_c - h)^2}{E_x^{(m)} h_m}}{d} - \frac{2v_{xy}^{(c)} h_c}{E_x^{(c)}}\right) + 2\,h_c, \tag{20}$$

$$C = -\frac{2G}{d}\left(\frac{1}{Ex^{(m)}}\frac{h_c}{h_m} + \frac{1}{E_x{}^{(c)}}\right) \,, \tag{21}$$

$$D = \frac{-G}{d}\left(\left[\frac{1}{Ex^{(m)}}\frac{h}{h_m}\sigma x\right] + (\alpha_m - \alpha_c)\Delta T\right), \tag{22}$$

Differentiating Eq. (18) with respect to x, and defining $\xi = B/A$, $\eta = C/A$ and $\theta = D/A$ the result becomes

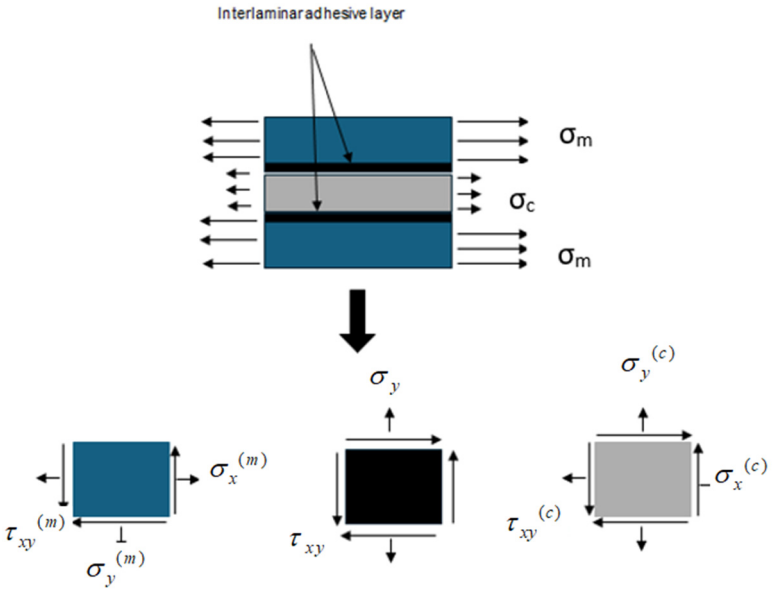

Figure 2. Stress component in the corresponding layer

$$\phi'''' + \xi\phi'' + \eta\phi = 0 \ , \tag{23}$$

The solution to Eq. (23) is obtained by solving the following characteristic equation

$$\lambda^4 + \xi\lambda^2 + \eta = 0, \tag{24}$$

Finally

$$\phi = \frac{\theta}{\eta} + C_1 e^{-ax} + C_2 e^{ax} + C_3 e^{-bx} + C_4 e^{bx}, \tag{25}$$

With

$$C_1 = \frac{1}{2} \cdot \frac{b \cdot sin(b \cdot S) \cdot \theta}{\eta(\cosh(b \cdot S) \cdot a \cdot \sinh(a \cdot S) - b \cdot \sinh(b \cdot S) \cdot \cosh(a \cdot S))}, \tag{26}$$

$$C_2 = \frac{1}{2} \cdot \frac{b \cdot sin(b \cdot S) \cdot \theta}{\eta(\cosh(b \cdot S) \cdot a \cdot \sinh(a \cdot S) - b \cdot \sinh(b \cdot S) \cdot \cosh(a \cdot S))}, \tag{27}$$

$$C_3 = -\frac{1}{2} \cdot \frac{a \cdot sin(a \cdot S) \cdot \theta}{\eta(\cosh(b \cdot S) \cdot a \cdot \sinh(a \cdot S) - b \cdot \sinh(b \cdot S) \cdot \cosh(a \cdot S))}, \tag{28}$$

$$C_4 = -\frac{1}{2} \cdot \frac{asin(a \cdot S) \cdot \theta}{\eta(\cosh(b \cdot S) \cdot a \cdot \sinh(a \cdot S) - b \cdot \sinh(b \cdot S) \cdot \cosh(a \cdot S))}, \tag{29}$$

$$a = \frac{1}{2} \cdot \sqrt{-2 \cdot \xi - 2 \cdot \sqrt{\xi^2 - 4\eta}} \ , \tag{30}$$

$$b = \frac{1}{2} \cdot \sqrt{-2 \cdot \xi + 2 \cdot \sqrt{\xi^2 - 4\eta}}\,, \tag{31}$$

Finally, the stress functions that satisfy the boundary conditions, equilibrium equations, and traction continuity at the interfaces can be determined. In this model, it is assumed that the inter-laminar adhesive layer has a thickness equal to twice the fiber diameter (with the fiber diameter assumed to be 7.6 μm) [18]. As a result, the values of ($\nu_m - \nu_c$) in Eq. (15) and ($u_m - u_c$) in Eq. (16) are approximately zero.

The stresses in an undamaged sandwich, along with its stiffness matrix, can be determined using classical laminate theory. The stress-strain relationships for the constituent materials are as follows [10]

For the metal layer

$$\varepsilon_x = \frac{1}{E_m}\sigma_{xm} - \frac{\upsilon_m}{E_m}\sigma_{ym} - \frac{\upsilon_m}{E_m}\sigma_{zm}, \tag{32}$$

$$\varepsilon_y = -\frac{\upsilon_m}{E_c}\sigma_{xm} + \frac{1}{E_c}\sigma_{ym} - \frac{\upsilon_c}{E_c}\sigma_{zm}, \tag{33}$$

For the ceramic layer

$$\varepsilon_x = \frac{1}{E_c}\sigma_{xc} - \frac{\upsilon_m}{E_m}\sigma_{yc} - \frac{\upsilon_c}{E_c}\sigma_{zc}, \tag{34}$$

$$\varepsilon_y = -\frac{\upsilon_m}{E_c}\sigma_{xc} + \frac{1}{E_m}\sigma_{yc} - \frac{\upsilon_m}{E_m}\sigma_{zc}, \tag{35}$$

For the axis systems (x,y,z), (x_m,y_m,z_m), (x_c,y_c,z_c), please refer to Fig. 2.

It is assumed that a generalized state of plane strain is achieved such that the average strain along the y-axis is the same in both layers, and that ε_y remains constant.

$$\varepsilon_y = \overline{\varepsilon_{ym}} = \overline{\varepsilon_{yc}}, \tag{36}$$

To obtain the Poisson's ratio for a damaged laminate, the following parameters must be calculated

$$\upsilon_{xy} = -\frac{\varepsilon_y}{\overline{\varepsilon_{xm}}}, \tag{37}$$

This equation includes the average value of the crack opening displacement normalized by the far-field strain ε_{xm}. Therefore, the average transverse crack opening displacement, denoted as u_a, is required.

$$u_a = s(\overline{\varepsilon_{xm}} - \overline{\varepsilon_{xc}}), \tag{38}$$

To utilize definitions Eq. (37) and (38), the average strains involved are expressed in terms of the applied load σ_{xm}. Since the problem is treated as linear, all strains are proportional to the load. Consequently, Eq. (39) includes only the elastic and geometric properties of the constituents, the crack density, and the normalized crack opening within the laminate. The crack opening will be derived from the stress distributions surrounding the crack. After formulating the equilibrium equations for forces in the y and z directions, the following results are obtained

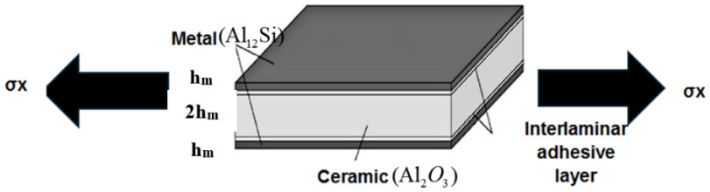

Figure 3. A Geometric model for a Metal/Ceramic sandwich plate with transverse cracks

$$\varepsilon_y = -\frac{\upsilon_{12}}{E_m(E_m h_c + E_c h_m)}\left(E_m h_c \overline{\sigma_{xc}} + E_c h_m \overline{\sigma_{xm}}\right), \tag{39}$$

Thus, this strain component is dependent on the average stress along the x-axis in both layers. By averaging the constitutive relationships (34) to (37), the following is obtained

For the metal layer

$$\overline{\varepsilon_{xm}} = \frac{1}{E_m}\overline{\sigma_{xm}} - \frac{\upsilon_m}{E_m}\overline{\sigma_{ym}}, \tag{40}$$

$$\varepsilon_{ym} = -\frac{\upsilon_m}{E_m}\overline{\sigma_{xm}} + \frac{1}{E_c}\overline{\sigma_{ym}}, \tag{41}$$

For the ceramic layer

$$\overline{\varepsilon_{xc}} = \frac{1}{E_c}\overline{\sigma_{xc}} - \frac{\upsilon_m}{E_m}\overline{\sigma_{yc}}, \tag{42}$$

$$\varepsilon_{yc} = -\frac{\upsilon_m}{E_m}\overline{\sigma_{xc}} + \frac{1}{E_m}\overline{\sigma_{yc}}, \tag{43}$$

3. Results and discussion

A computer code based on the present model was developed to predict the mechanical behavior of the porous and cracked sandwich plate under thermo-mechanical loading.

3.1 Validation of the present model

Consider a sandwich plate composed of two distinct layers: the first layer consists of $Al_{12}Si$ aluminium alloy, while the second layer is made of Al_2O_3 (alumina), which is assumed to be fully dense and free of porosity, as illustrated in Fig. 3. The material properties for both layers are provided in Table 1.

Fig. 4 illustrates the distribution of the normalized axial stress σ_{xx}/σ_x under uniaxial tensile loading as a function of x coordinate, considering various half-spacing-to-layer thickness ratios (s/h_c, where h_c represents the thickness of the ceramic layer / see Fig. 1). According to the analytical model, the average axial stress between adjacent cracks remains tensile, with its magnitude decreasing as the spacing between neighboring cracks is reduced. A strong correlation is observed between the results of the present model and those of the 2D shear lag model proposed by Kashtalyan et al. [14], demonstrating the validity of the approach.

Table 1. Properties of the constituents [14]

Constituent	Young's modulus (GPa)	Poisson's ratio	Layer thickness (mm)	Shear modulus (GPa)	thermal expansion coefficient (K^{-1})
Aluminium alloy $Al_{12}Si$	80	0.33	0.3	30	$19.6 \cdot 10^{-6}$
Alumina Al_2O_3	390	0.24	0.2	157.26	$8.68 \cdot 10^{-6}$

Table 2. Comparison of stiffness degradation with Equivalent Constraint Model as a function of crack density with different ceramic ratio percentage

Pc (%)	Damage density (1/mm)	Present model	ECM Kashtalyan et al. [14]	|Error (%)|
35%	0.1	0.80559	0.79851	0.7080 %
	0.2	0.67446	0.6664	0.8060 %
	0.3	0.58005	0.57155	0.8500 %
	0.4	0.50884	0.50379	0.5050 %
	0.5	0.45333	0.44959	0.3740 %
	0.6	0.40911	0.40556	0.3550 %
	0.7	0.37345	0.37507	0.1620 %
	0.8	0.34449	0.34797	0.3480 %
	0.9	0.32088	0.33442	1.3540 %
45%	0.1	0.79093	0.76735	2.3580 %
	0.2	0.65416	0.63265	2.1510 %
	0.3	0.55786	0.5551	0.2760 %
	0.4	0.48724	0.4898	0.2560 %
	0.5	0.43487	0.44898	1.4110 %
	0.6	0.3961	0.41633	2.0230 %
	0.7	0.36745	0.39184	2.4390 %
	0.8	0.34625	0.37959	3.3340 %
	0.9	0.33047	0.36327	3.2800 %

Furthermore, Table 2 compares the stiffness degradation predicted by the present model with that obtained from the Equivalent Constraint Model (ECM). The results exhibit excellent agreement across a wide range of damage densities and ceramic volume fractions, particularly for Pc = 35%, where the maximum deviation is below 1.5%. A maximum stiffness reduction of approximately 68% is observed at a crack density of 0.9 (1/mm), highlighting the significant influence of transverse cracks on the composite's structural rigidity. These comparisons confirm that the proposed model accurately predicts stiffness degradation trends and stress distribution behavior, providing a robust framework for analyzing cracked and porous metal–ceramic composites.

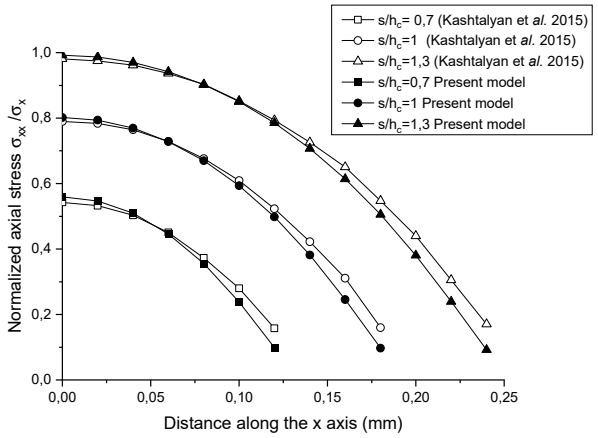

Figure 4. Normalised axial stress σ_{xx}/σ_x in the ceramic layer as a function of coordinate x for a range of crack spacing-to-layer thickness ratios

3.2 Thermo-mechanical behavior of the porous Al-12Si / Al_2O_3

The thermo-mechanical response of the Al-12Si/Al_2O_3 sandwich plate was analyzed by integrating the effect of porosity using an established empirical relationship. This model expresses the reduction in elastic and shear moduli of the porous ceramic as a function of the pore-volume fraction, while maintaining good computational efficiency. It realistically represents stiffness degradation in porous ceramics such as Al_2O_3, where pore geometry and connectivity strongly influence the effective properties.

For the Young's modulus of the porous ceramic layer

$$E_c = E_{c0}(1 - V_p)^n, \tag{44}$$

Where, E_{c0} is the Young's modulus of the dense ceramic (without pores), V_p is the volume fraction of pores and n is an empirical parameter depending on the pore structure.

- For randomly distributed spherical pores: $n \approx 2$
- For interconnected or elongated pores : $n \approx 3-4$

For shear modulus of the porous ceramic layer

$$G_c = G_{c0}(1 - V_p)^n \,, \tag{45}$$

Where, G_{c0} is the shear modulus of the dense ceramic (without pores), V_p is the volume fraction of pores and n is an empirical parameter depending on the pore structure.

For Poisson's ratio of the porous ceramic layer, it is less affected by porosity than E_c and G_c. A common approximation is

$$\nu_c = \nu_{c0}\left(1 - V_p\right)^n. \tag{46}$$

Where, ν_{c0} is the Poisson's ratio of the dense ceramic (without pores), V_p is the volume fraction of pores and n is an empirical parameter depending on the pore structure.

Table 3. Distribution of interlaminar normal stress in Al-12Si/Al_2O_3 metal/ceramic with different thermal stresses and different volume fraction ceramic and porosity ($\sigma_x = 500\ MPa$)

Pr (%)	Pc (%)	x/s	Interlaminar Normal Stress σ_y (Mpa)			
			ΔT=0°C	ΔT=250°C	ΔT=450°C	Relative Gap $\left\|\frac{\sigma_y(\Delta T=0°C)-\sigma_y(\Delta T=450°C)}{\sigma_y(\Delta T=0°C)}\right\|$
0%	10%	0.0	592.76	591.60	590.67	0.35%
		0.2	527.81	526.78	525.95	
		0.4	327.86	327.22	326.70	
		0.6	-22.83	-22.78	-22.75	
		0.8	-551.83	-550.75	-549.88	
		1.0	-1300.75	-1298.20	-1296.17	
	50%	0.0	493.32	492.78	492.35	0.20%
		0.2	435.47	434.99	434.62	
		0.4	260.77	260.49	260.26	
		0.6	-34.23	-34.19	-34.16	
		0.8	-455.36	-454.87	-454.47	
		1.0	-1010.96	-1009.86	-1008.98	
30%	10%	0.0	329.24	328.60	328.08	0.35%
		0.2	291.35	290.78	290.33	
		0.4	176.31	175.97	175.69	
		0.6	-20.01	-19.97	-19.94	
		0.8	-304.68	-304.09	-303.61	
		1.0	-687.95	-686.60	-685.52	
	50%	0.0	249.75	249.48	249.26	0.20%
		0.2	220.10	219.86	219.67	
		0.4	130.88	130.73	130.62	
		0.6	-18.75	-18.72	-18.71	
		0.8	-230.13	-229.88	-229.68	
		1.0	-505.23	-504.68	-504.25	

3.2.1 Normal stress distribution of porous Al-12Si/Al_2O_3

3.2.1.1 Thermal stresses effect on the normal stress distribution of porous Al12Si/Al_2O_3

Table 3 presents the interlaminar normal stress for various porosity (Pr) and ceramic-volume fractions (Pc) under different thermal loads. The results indicate that the normal stress decreases with increasing temperature and porosity because both factors lower the composite's effective stiffness and load-bearing capacity. The thermal mismatch between Al-12Si and Al_2O_3 also generates residual stresses, though the relative stress variation remains small (≤ 0.35%), confirming good thermal stability. Maximum tensile and compressive stresses appear at x/S = 0 and x/S = 1, respectively, following a nearly symmetrical pattern. These results demonstrate that the composite maintains mechanical integrity even at elevated temperatures, which is favorable for high-temperature applications.

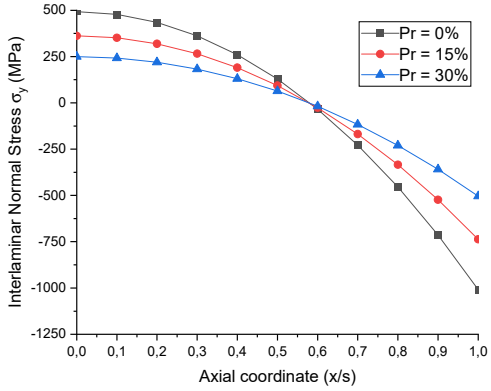

Figure 5. Interlaminar normal stress in the ceramic layer as a function of coordinate x for different porosity volume fraction (ΔT=450°C and P_c = 50%)

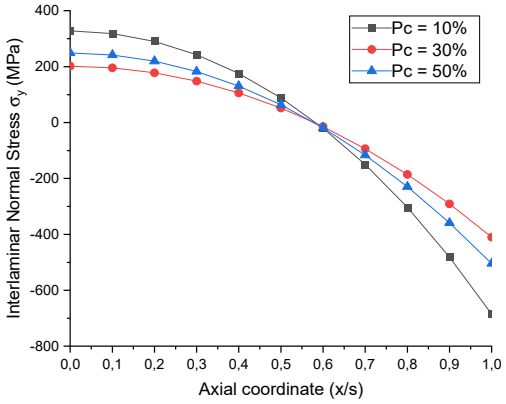

Figure 6. Interlaminar normal stress in the ceramic layer as a function of coordinate x for different ceramic volume fraction (ΔT=450°C and P_r = 30%)

The stress distribution through the thickness is affected by both porosity and temperature. Higher porosity reduces stiffness and smooths the stress gradient, while elevated temperature amplifies interfacial stresses due to thermal-expansion mismatch. These coupled effects control the composite's overall thermo-mechanical stability.

3.2.1.2 Porosity and ceramic proportion effect on the normal stress distribution of porous Al-12Si/Al_2O_3

Fig. 5 shows that the interlaminar normal stress in the ceramic layer transitions from tension to compression near the damaged plane (x/S). This transition becomes more pronounced as porosity increases, since pores weaken the material's ability to transmit load, resulting in lower stress magnitudes. The tensile region (x/S < 0.6) corresponds to matrix stretching, whereas the compressive region (x/S > 0.6) arises from stress redistribution around the crack.

Table 4. Distribution of interlaminar shear stress in Al-12Si/Al_2O_3 metal/ceramic with different thermal stresses and a different volume fraction ceramic and porosity ($\sigma_x = 500\ MPa$)

Pr (%)	Pc (%)	x/s	Interlaminar Shear Stress τ_{xy} (Mpa)			
			ΔT=0°C	ΔT=250°C	ΔT=450°C	Relative Gap $\left\|\frac{\tau_{xy}(\Delta T=0°C)-\tau_{xy}(\Delta T=450°C)}{\tau_{xy}(\Delta T=0°C)}\right\|$
0%	10%	0.0	0.0000	0.0000	0.0000	0.35%
		0.2	0.3046	0.3040	0.3035	
		0.4	0.5391	0.5380	0.5372	
		0.6	0.6276	0.6264	0.6254	
		0.8	0.4831	0.4821	0.4814	
		1.0	0.0000	0.0000	0.0000	
	50%	0.0	0.0000	0.0000	0.0000	0.20%
		0.2	0.2528	0.2526	0.2523	
		0.4	0.4437	0.4433	0.4429	
		0.6	0.5096	0.5091	0.5086	
		0.8	0.3848	0.3844	0.3841	
		1.0	0.0000	0.0000	0.0000	
30%	10%	0.0	0.0000	0.0000	0.0000	0.35%
		0.2	0.1689	0.1685	0.1683	
		0.4	0.2971	0.2965	0.2960	
		0.6	0.3425	0.3418	0.3413	
		0.8	0.2600	0.2595	0.2591	
		1.0	0.0000	0.0000	0.0000	
	50%	0.0	0.0000	0.0000	0.0000	0.20%
		0.2	0.1279	0.1278	0.1277	
		0.4	0.2242	0.2239	0.2237	
		0.6	0.2568	0.2565	0.2563	
		0.8	0.1932	0.1930	0.1928	
		1.0	0.0000	0.0000	0.0000	

Fig. 6 illustrates that the ceramic-volume fraction also influences stress distribution. Higher Pc values increase stiffness and amplify stress magnitude, while lower Pc values lead to more uniform but smaller stress levels dominated by the ductile metal matrix. The intermediate composition (Pc = 50%) provides a balanced stress transfer, limiting localization while maintaining strength.

3.2.2 Shear stress distribution of porous Al-12Si/Al_2O_3

3.2.2.1 Thermal stresses effect on the shear stress distribution of porous Al-12Si/Al_2O_3

Table 4 summarizes the interlaminar shear stress (τ_{xy}) for various porosity and ceramic fractions under different temperature conditions. The results show that τ_{xy} decreases with increasing temperature and porosity because both factors reduce the effective stiffness and weaken

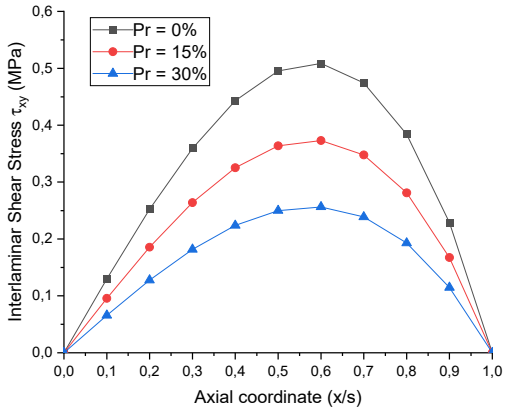

Figure 7. Interlaminar shear stress in the ceramic layer as a function of coordinate x for different porosity volume fraction (ΔT=450°C and P_c = 50%)

stress transfer between layers. At higher ceramic content, the composite exhibits greater rigidity and thus higher peak shear stresses, but the presence of porosity counteracts this effect by disrupting load continuity. The shear stress reaches its maximum around x/s = 0.6 and drops to zero near the damage plane, in agreement with boundary conditions. The relative change in shear stress remains minimal (≤ 0.35%), confirming that the composite retains good thermal stability. This interaction between reinforcement, porosity, and temperature demonstrates the material's capacity to maintain mechanical integrity under service conditions.

3.2.2.2 Porosity and ceramic proportion effect on the shear stress distribution of porous Al-12Si/Al_2O_3

Fig. 7 illustrates that increasing porosity significantly reduces interlaminar shear stress throughout the ceramic layer. This reduction results from diminished stiffness and impaired load-transfer efficiency caused by pores within the structure. The peak shear stress consistently occurs near x/S = 0.6 and approaches zero at the crack plane, reflecting symmetrical load redistribution. This behavior emphasizes the interdependence between porosity, shear stress distribution, and the overall mechanical stability of the material.

Fig. 8 shows the influence of ceramic content (Pc) on τ_{xy}. Higher ceramic fractions enhance stiffness and lead to greater shear stress magnitudes, while lower Pc values result in smoother, less localized stress profiles dominated by the metallic phase. The intermediate composition (Pc = 50%) provides an optimal compromise, ensuring effective stress transfer without excessive concentration, which is advantageous for maintaining overall structural stability.

3.2.3 Young's modulus distribution of porous Al-12Si/Al_2O_3

3.2.3.1 Thermal stresses effect on the Young's modulus of porous Al-12Si/Al_2O_3

Table 5 presents the variation of Young's modulus (Ex) for different porosity and ceramic fractions under varying temperature conditions. The results show that Ex decreases with increasing temperature due to thermal softening of both phases. The reduction is more significant at higher ceramic contents, where stiffness is initially greater but more sensitive to temperature gradients.

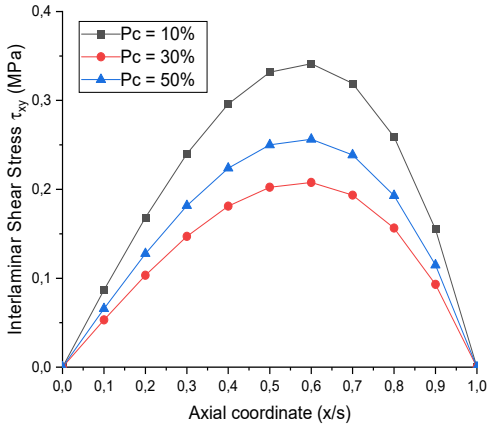

Figure 8. Interlaminar shear stress in the ceramic layer as a function of coordinate x for different ceramic volume fraction (ΔT=450°C and P_r = 30%)

For example, at Pc = 50% and Pr = 0%, Ex decreases from 117.5 GPa at ΔT = 0°C to 112.15 GPa at ΔT = 450°C (a 4.55% drop), while for Pc = 10%, the reduction is less than 1%. The presence of porosity amplifies this effect, since pores act as stress-relief sites, further reducing the effective modulus. These results confirm that ceramic reinforcement improves initial stiffness but simultaneously increases thermal sensitivity when porosity is present.

Although temperature and porosity are discussed separately for clarity, the model simultaneously considers their combined influence. The porosity-dependent moduli are integrated within the temperature-dependent constitutive relations, ensuring coupled thermo-porous effects. This approach accurately represents the composite's overall stiffness degradation behavior.

3.2.3.2 Porosity and ceramic proportion effect on the Young's modulus of porous Al-12Si/Al_2O_3

According to Fig. 9, the Young's modulus (E_x) decreases markedly with increasing porosity, reflecting the strong impact of voids on load transfer and stiffness degradation. For Pc = 50%, Ex drops from 67.77 GPa at Pr = 0% to 28.06 GPa at Pr = 100%, corresponding to a 58.6% reduction. At lower Pc values (e.g., 10%), the decrease is less severe, confirming that porosity predominantly affects the ceramic-rich regions where rigidity is highest. This behavior indicates that porosity disrupts load transfer within the material, leading to reduced stress transmission and accelerated stiffness degradation. The findings emphasize that increased porosity severely deteriorates the mechanical performance of the composite, establishing it as a key factor influencing its thermo-mechanical stability.

As shown in Fig. 10, the Young's modulus (E_x) initially increases with ceramic volume fraction (Pc) due to the higher stiffness of the ceramic phase. At moderate porosity (Pr = 30%), Ex increases from 45.56 GPa at Pc = 10% to 67.77 GPa at Pc = 50%, indicating a 48.7% gain. However, beyond a crack density of 0.5, the reinforcement effect diminishes as damage-induced stress relaxation offsets the stiffness contribution of the ceramic phase. This reveals an optimal ceramic fraction that balances reinforcement and damage resistance, maximizing stiffness without excessive stress concentration.

Table 5. Variation of Young's modulus in Al-12Si/Al2O3 metal/ceramic with different thermal stresses and different volume fraction of ceramic and porosity ($\sigma_x = 500\ MPa$)

Pr (%)	Pc (%)	Damage Density (1/mm)	Young's Modulus E_x (GPa)			
			ΔT=0°C	ΔT=250°C	ΔT=450°C	Relative Gap $\left\|\frac{E_x(\Delta T=0°C)-E_x(\Delta T=450°C)}{E_x(\Delta T=0°C)}\right\|$
0%	10%	0.0	55.50	55.21	54.98	0.94%
		0.2	52.29	52.06	51.87	0.79%
		0.4	49.42	49.24	49.10	0.65%
		0.6	46.86	46.73	46.62	0.53%
		0.8	44.60	44.50	44.42	0.42%
		1.0	42.68	42.60	42.54	0.33%
	50%	0.0	117.50	114.47	112.15	4.55%
		0.2	72.31	71.29	70.50	2.50%
		0.4	52.22	51.77	51.41	1.55%
		0.6	40.95	40.71	40.53	1.01%
		0.8	33.96	33.83	33.73	0.68%
		1.0	29.49	29.41	29.35	0.46%
30%	10%	0.0	45.56	45.44	45.34	0.47%
		0.2	44.46	44.36	44.28	0.41%
		0.4	43.42	43.33	43.26	0.36%
		0.6	42.42	42.35	42.29	0.31%
		0.8	41.47	41.41	41.36	0.27%
		1.0	40.58	40.53	40.49	0.22%
	50%	0.0	67.77	66.91	66.23	2.28%
		0.2	52.47	52.01	51.65	1.56%
		0.4	42.80	42.54	42.33	1.10%
		0.6	36.16	36.01	35.88	0.78%
		0.8	31.43	31.33	31.26	0.56%
		1.0	28.06	28.00	27.95	0.39%

3.2.4 Poisson's ratio distribution of porous Al-12Si/Al_2O_3

3.2.4.1 Thermal stresses effect on the Poisson's ratio of porous Al-12Si/Al_2O_3

The Poisson's ratio (ν_x) decreases with increasing temperature (ΔT) due to thermal expansion effects, with more pronounced drop at higher porosity (Pr) (see Table 6). The results show that νx decreases with increasing temperature due to thermal expansion effects, which reduce lateral deformation resistance. The reduction is more pronounced at low porosity, where the material retains higher stiffness and transmits greater thermal stresses. For instance, at Pc = 50% and Pr = 0%, νx decreases from 0.5477 at ΔT = 0°C to 0.5326 at ΔT = 450°C, while at Pr = 50%, it drops from 0.4652 to 0.4577. This trend confirms that porosity mitigates temperature-induced effects by

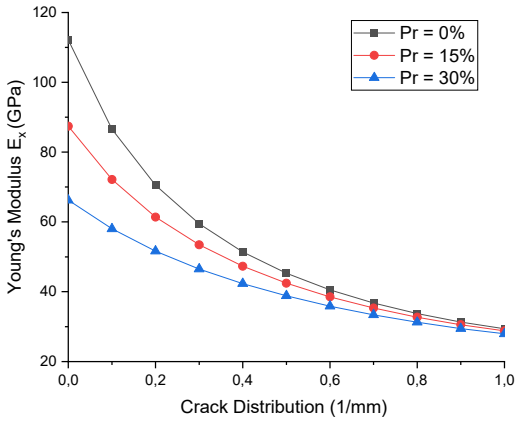

Figure 9. Young's modulus in metal/ceramic Al-12Si/Al_2O_3 as a function of crack distribution and for different porosity volume fraction (ΔT=450°C and P_c = 50%)

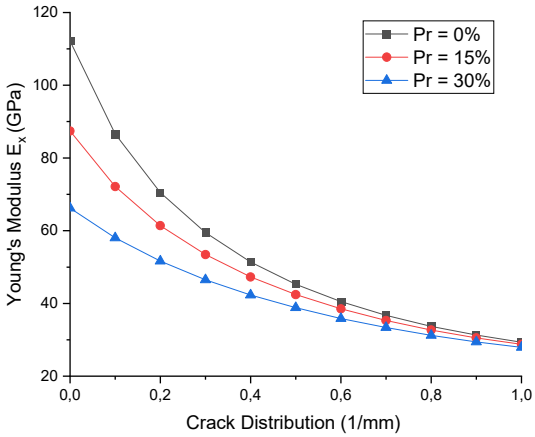

Figure 10. Young's modulus in metal/ceramic Al-12Si/Al_2O_3 as a function of crack distribution and for different ceramic volume fraction (ΔT=450°C and P_r = 30%)

lowering the effective modulus. Overall, the combined influence of porosity and temperature determines the material's lateral strain response and its ability to maintain dimensional stability under thermo-mechanical loading.

3.2.4.2 Porosity and ceramic proportion effect on the Poisson's ratio of porous Al-12Si/Al_2O_3

Fig. 11 shows that νx decreases markedly with increasing porosity, indicating that voids weaken lateral stiffness and promote local deformation. For Pc = 50%, νx falls from 0.5477 at Pr = 0% to 0.3005 at Pr = 100%, corresponding to a 45% reduction. At lower ceramic content, the metallic phase dominates, resulting in a higher initial νx and greater ductility.

Table 6. Variation of Poisson's ratio in Al-12Si/Al2O3 metal/ceramic with different thermal stresses and a different volume fraction ceramic and porosity

Pr (%)	Pc (%)	Damage Density (1/mm)	Poisson's Ratio ν_{xy}			
			ΔT=0°C	ΔT=250°C	ΔT=450°C	Relative Gap $\left\|\frac{\upsilon_{xy}(\Delta T=0°C)-\upsilon_{xy}(\Delta T=450°C)}{\upsilon_{xy}(\Delta T=0°C)}\right\|$
0%	10%	0.0	0.3585	0.3537	0.3498	0.87%
		0.2	0.3053	0.3015	0.2985	0.68%
		0.4	0.2580	0.2550	0.2526	0.53%
		0.6	0.2156	0.2133	0.2115	0.41%
		0.8	0.1782	0.1765	0.1751	0.31%
		1.0	0.1464	0.1451	0.1441	0.23%
	50%	0.0	0.5477	0.5391	0.5326	1.50%
		0.2	0.4207	0.4179	0.4157	0.51%
		0.4	0.3643	0.3631	0.3621	0.23%
		0.6	0.3327	0.3320	0.3315	0.12%
		0.8	0.3130	0.3127	0.3124	0.06%
		1.0	0.3005	0.3003	0.3001	0.04%
30%	10%	0.0	0.3504	0.3465	0.3434	0.70%
		0.2	0.3143	0.3109	0.3082	0.60%
		0.4	0.2798	0.2769	0.2747	0.52%
		0.6	0.2470	0.2445	0.2426	0.44%
		0.8	0.2157	0.2136	0.2120	0.37%
		1.0	0.1861	0.1845	0.1832	0.30%
	50%	0.0	0.4652	0.4610	0.4577	0.75%
		0.2	0.3907	0.3885	0.3867	0.40%
		0.4	0.3436	0.3424	0.3413	0.23%
		0.6	0.3113	0.3106	0.3099	0.14%
		0.8	0.2883	0.2878	0.2874	0.09%
		1.0	0.2719	0.2716	0.2713	0.05%

The Poisson's ratio (ν_x) increases as the ceramic volume fraction (Pc) increases, due to higher crack density and porosity within the ceramic layer (Fig. 12). At constant porosity (Pr = 30%), νx increases from 0.2719 at Pc = 10% to 0.3504 at Pc = 50%, a 28.9% rise. This behavior is attributed to the stiffer ceramic phase becoming more prone to microcracking and localized deformation as its proportion increases. Consequently, higher ceramic fractions enhance lateral strain while improving stiffness, demonstrating the complex interaction between reinforcement, porosity, and damage in the composite structure.

4. Conclusions

This study provides a predictive model for the thermo-mechanical behavior of Al-12Si/Al_2O_3 composites, addressing the influence of porosity and ceramic content on stress distribution and

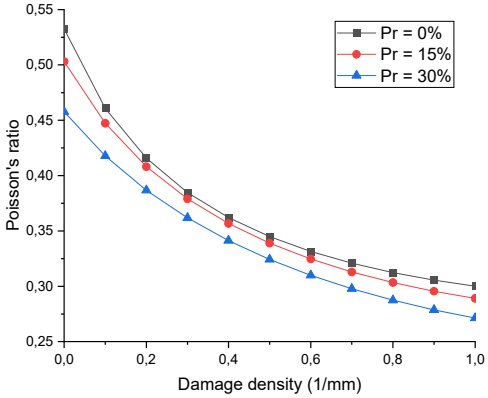

Figure 11. Poisson's ratio in metal/ceramic Al-12Si/Al_2O_3 as a function of crack distribution and for different porosity volume fraction (ΔT=450°C and P_c = 50%)

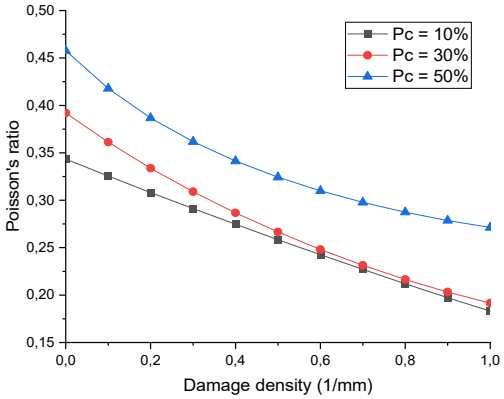

Figure 12. Poisson's ratio in metal/ceramic Al-12Si/Al_2O_3 as a function of crack distribution and for different ceramic volume fraction (ΔT=450°C and P_r = 30%)

mechanical behavior. It develops a theoretical model to predict stress distribution, Young's modulus and Poisson's ratio while incorporating the effects of porosity and ceramic content. To validate the proposed model, the results are compared with the Equivalent Constraint Model (ECM) by [14], showing strong agreement in stiffness degradation trends across different ceramic ratios. The stiffness reduction predicted by this study closely aligns with ECM predictions, confirming the accuracy and reliability of the approach. This validation reinforces the effectiveness of the model in predicting the mechanical response of metal-ceramic composites, particularly in the presence of porosity and thermal stresses. The originality of this work lies in its comprehensive investigation of the thermo-mechanical behavior of cracked and porous Al-12Si/Al_2O_3 metal-ceramic composites, integrating both stress distribution and material degradation under high-temperature conditions. Unlike previous studies that primarily focus on dense composites, this research uniquely considers the effects of porosity using Knudsen's model,

providing a more realistic representation of industrial materials. The detailed analysis of how porosity and ceramic content influence Young's modulus, Poisson's ratio, and interlaminar stress behavior under thermal loading further differentiates this work.

The stress distribution in porous Al-12Si/Al_2O_3 composites is significantly influenced by temperature, porosity, damage density and ceramic content, with stress transitioning from tensile to compressive near the damage plane. Higher porosity weakens stress transfer, reducing interlaminar normal and shear stress, while increased ceramic content enhances stress localization. Young's modulus decreases with increasing temperature and porosity, with a maximum reduction of 58.6% at 30% of porosity, highlighting the impact of voids on stiffness. However, higher ceramic content improves initial stiffness but also increases sensitivity to thermal degradation. Poisson's ratio decreases with rising temperature and porosity, confirming a weakened lateral deformation resistance in more porous structures. Notably, higher ceramic content increases Poisson's ratio due to microcrack formation, leading to greater lateral strain effects.

The purpose of this work is to develop a predictive model for the thermo-mechanical behavior of porous Al-12Si/Al_2O_3 metal-ceramic composites, aiding in the optimization of their mechanical performance for high-temperature applications. Future studies will focus on fatigue behavior under cyclic thermal loading and further validation using experimental testing. Additionally, optimizing material composition for specific aerospace and automotive applications remains a key goal.

References

1. Scherm, F., Völkl, R., Neubrand, A., Bosbach, F., Glatzel, U. (2010). Mechanical characterisation of interpenetrating network metal ceramic composites. Materials Science and Engineering A, 527, 1260-1265. https://doi.org/10.1016/j.msea.2009.09.063.
2. Schukraft, J., Roßdeutscher J., Siegmund, F., Weidenmann, K.A. (2022). Thermal expansion behavior and elevated temperature elastic properties of An interpenetrating metal/ceramic composite. Thermochimica Acta, 715, 179298. https://doi.org/10.1016/j.tca.2022.179298.
3. Kota, N., Sai Charan, M., Laha, T., Roy, S. (2022). Review on development of metal/ceramic interpenetrating phase composites and critical analysis of their properties. Ceramics International, 48(2), 1451-1483. https://doi.org/10.1016/j.ceramint.2021.09.232.
4. Gudlur, P., Forness, A., Lentz, J. (2012). Thermal and mechanical properties of Al/Al2O3 composites at elevated temperatures. Materials Science and Engineering A, 531, 18-27. https://doi.org/10.1016/j.msea.2011.10.001.
5. Sharma, N.K., Mishra, R.K., Sharma, S. (2016). 3D micromechanical analysis of thermo-mechanical behavior of Al2O3/Al metal matrix composites. Computational Materials Science, 115, 192-201. https://doi.org/10.1016/j.commatsci.2015.12.051.
6. Wei, H., Li, C., Xu, Y., Zhang, X., Li, J., Han, Y., Li M., Xu X. (2024). Aluminum-based ceramic/metal composites with tailored thermal expansion fabricated by spark plasma sintering. Royal Society of Chemistry Advances, 14, 3952-3961. https://doi.org/10.1039/D3RA07593A.
7. Kursa, M., Kowalczyk-Gajewska, K., Petryk H. (2014). Multi-objective optimization of thermo-mechanical properties of metal–ceramic composites. Composites Part B: Engineering, 60, 586-596. https://doi.org/10.1016/j.compositesb.2014.01.009.
8. Bhat, C., Jiang, C.P., Shan Romario, Y., Paral, S.K., Toyserkani, E. (2024). Critical review of metal-ceramic composites fabricated additive manufacturing for extreme condition applications. Mechanics of Advanced Materials and Structures, 32(10), 1-28. https://doi.org/10.1080/15376494.2024.2376337.
9. Shekhawat, D., Singh A., Patnaik, A., (2023). Effect of ceramic reinforcement on physical and mechanical behaviour of AL6061 metal matrix composites fabricated using stir casting technique.

International Journal of Metalcasting, 17, 2207-2225. https://doi.org/10.1007/s40962-022-00926-2.
10. Khodjet-Kesba, M., EL Meiche N., Benkhedda, A. (2021). Stress distribution on the cracked sandwich plate with non linear thermal and moisture concentration. Nano Hybrids and Composites, 32, 45-62. https://doi.org/10.4028/www.scientific.net/NHC.32.45.
11. Maizia, A., Hocine, A., Dehmous, H., Chapelle, D. (2017). Prediction of reliability analysis of composite tubular structure under hygro-thermo-mechanical loading. Mechanics of Advanced Materials and Structures, 26(4), 372-379. https://doi.org/10.1080/15376494.2017.1387329.
12. Kim, S.J., Han, S.Y., Shin, E.S. (2013). Micromechanics-based evaluation of the poroelastic effect and stress concentration in thermochemically-decomposed composites. Journal of Mechanical Science and Technology, 27, 3139-3147. https://doi.org/10.1007/s12206-013-0834-z.
13. Shi, S., Gu, L., Liang, J., Fang, G., Gong, C., Dai, C. (2016). A mesomechanical model for predicting the degradation in stiffness of FRP composites subjected to combined thermal and mechanical loading. Materials & Design, 89, 1079-1085. https://doi.org/10.1016/j.matdes.2015.10.060.
14. Kashtalyan, M., Sinchuk, Y., Piat, R., Guz I. (2015). Analysis of multiple cracking in metal/ceramic composites with lamellar microstructure. Archive of Applied Mechanics, 86, 177-188. https://doi.org/10.1007/s00419-015-1103-7.
15. Lekhnitskii, S.G. (1968). Anisotropic plates. Gordon and Breach, Science publishers, Ins. 150 Fifth Avenue, New York, N.Y., 10011.
16. El Meiche, N., Tounsi, A., Adda-Bedia, E.A., Megueni, A. (2009). Analysis of the transverse cracking in hybrid cross-ply composite laminates. Computational Materials Science, 46(4), 1102-1108. https://doi.org/10.1016/j.commatsci.2009.05.019.
17. Laws, N., Dvorak, G. (1988). Progressive transverse cracking in composite laminates. Journal of Composite Materials, 22(10), 900-916. https://doi.org/10.1177/002199838802201001.
18. Highsmith, A.L., Reifsnider, K.L. (1982). Damage in composite materials: basic mechanisms, accumulation, tolerance, and characterization. ASTM Special Technical Publication 775. publication code number 04-775000-30, 1916 Race street, Philadelphia 19103, USA.